Discovery of quasi-six-coordinated layered phase of PBr_3 at high temperature and pressure

Jinqun Cai,[1] Siyu Liu,[1] Wencheng Lu,[1] Yunqi Ji,[1,2] Kun Hao,[1] Xingxing Zhao,[1] Ping Ning,[1] Guangtao Liu,[1,*] Hongbo Wang,[1,†] and Mi Zhou[1,‡]

[1]*Key Laboratory of Material Simulation Methods & Software of Ministry of Education and State Key Laboratory of Superhard Materials, College of Physics, Jilin University, Changchun 130012, China*

[2]*International Center of Future Science, Jilin University, Changchun 130012, China*

(Received 21 April 2023; revised 7 July 2023; accepted 4 August 2023; published 7 September 2023)

Layered trihalides, mainly formed by metal elements and halogens, are promising candidates for spintronic devices and van der Waals heterostructures, but are rarely found in nonmetal halides. Motivated by the purpose of searching for the compelling layered configuration in a covalent system, we performed systemically high-pressure experiments to explore the crystal structures in typical PBr_3 with diamond anvil cell technique. At room temperature, PBr_3 crystallizes into a molecular crystal with orthorhombic symmetry above 0.9 GPa and is found to persist up to at least 43.9 GPa as confirmed by *in situ* Raman and x-ray diffraction measurements. Strikingly, a novel layered phase with a space group $P2_1/c$ is observed at ∼27.0 GPa and ∼1800 K, which is characterized by quasi-six-coordination of P atoms with nearby Br atoms. In addition, first-principles calculations indicate that the unusual coordination of the P atom in $P2_1/c$ phase is highly correlated with the pressure-induced generation of pnictogen bonds. Our current findings not only expand the understanding of the phase diagram of PBr_3, but also show an interesting transformation from molecular crystal to an extended layered phase achieved in a broad range of nonmetal trihalides.

DOI: 10.1103/PhysRevResearch.5.033164

I. INTRODUCTION

Molecular materials, characterized by strong intra- and weak intermolecular bonds, will tend to form extended three-dimensional geometries under extreme pressures, leading to intriguing phenomena such as phase transition [1–3], metallization [4,5], decomposition [6], disproportionation [7], and polymerization [8,9], thus providing fundamental knowledge in physics, chemistry, and planetary science. Recent reports reveal that high temperatures are pivotal for observing the above transformations owing to the kinetic barriers between different phases and chemical reactions during compression at room temperature, i.e., disproportionation of SO_2 [8] and phase transitions of CF_4 [10] and $SrOsO_3$ [11] were reported at high-pressure and high-temperature (HPHT) conditions, providing unequivocal experimental evidence for pursuing accurate energetic landscapes in simple molecular systems.

Group V elemental trihalides AX_3 (A = N, P, As, Sb, Bi; X = F, Cl, Br, I) are a family of simple four-atom compounds, which possess versatile applications in chemistry and materials fields [12–14]. Among them, the nitrogen, phosphorus, arsenate, and selenium trihalides usually adopt trigonal pyramidal geometry with C_{3v} point group symmetry, where A atom is sp^3 hybridized and overlaps with three halogen atoms to form covalent compounds AX_3 [15–21]. In contrast, ionic type compounds AX_3 such as BiI_3, where the metallic bismuth atom donates three p electrons to iodine atoms, tend to form a six-coordinated layered structure which is characterized by layers of bismuth ions that are octahedrally surrounded by six iodine ions so that they share edges with neighboring octahedra [21,22], the layers are stacked on top of one another with weak van der Waals bonding between adjacent layers. In addition CrI_3 and VI_3, which are isostructural to BiI_3, possess fascinating properties such as magnetic ordering and anisotropic electrical conductivity [23,24]. In previous reports, pressure has been confirmed to tune nonmetal into metal [25–28], which raises a scientific question about whether the trigonal pyramidal covalent compounds AX_3 could be transformed into a layered six-coordinated ionic structure under external compression.

In this paper, we present a pressure-induced structural evolution of PBr_3 by experimental and theoretical approaches up to 45.0 GPa. The *Pnma* phase of PBr_3 is formed at a freezing pressure of about 0.9 GPa and persists up to at least 43.9 GPa. Moreover, a layered phase (space group $P2_1/c$) with quasi-six-coordinated phosphorus is generated after laser heating at 27.0 GPa and is stable down to 1.5 GPa during decompression. Further first-principles calculations reveal that the generation of pnictogen bonds in $P2_1/c$ phase results in increased coordination of P atoms. The discovery broadens physical properties of PBr_3 and extends its potential applications as well as those of other two-dimensional functional materials. This study will pave a new avenue towards understanding the

*liuguangtao@jlu.edu.cn
†whb2477@jlu.edu.cn
‡mzhou@jlu.edu.cn

chemical bonding and compression mechanisms in AX_3 and expand the realm of two-dimensional functional materials in nonmetal trihalides.

II. METHODS

Phosphorus tribromide (PBr_3) (Alfa Aesar, purity 99%) was loaded into symmetric diamond anvil cells with a culet diameter of 200 μm. T-301 gasket was preindented to 20 μm thickness and a sample hole of 100 μm was drilled. The liquid sample and ruby pieces were loaded into the chamber in a glove box filled with argon. Pressures were determined using Raman shift of diamond anvil [29] and ruby [30] luminescence method. *In situ* x-ray diffraction (XRD) experiments were performed at the 4W2 beamline of the Beijing Synchrotron Radiation Facility (BSRF). Using a pair of Kirkpatrick-Baez mirrors to focus monochromatic synchrotron radiation x-ray beam with a wavelength of 0.6199 Å and spot size of $10 \times 30\,\mu m^2$. The two-dimensional (2D) x-ray diffraction patterns at different pressures were recorded by 2D imaging plate detector (MAR-3450). The instrument parameters were calibrated using a CeO_2 standard. The acquisition time of each 2D XRD pattern was 300 s. The integration and processing of 2D XRD patterns were carried out by using DIOPTAS program [31]. Rietveld refinements of XRD patterns were performed using GSAS II package [32]. Additionally, pressure dependencies of the unit-cell volume were fitted by the third-order Birch-Murnaghan equation of state (EOS) [33]. Raman spectra were collected using a homemade Raman instrument (Acton Standard Series SP-2556 Imaging Spectrograph and PyLoN:100BR_eXcelon CCD) with 632.8 nm excitation in backscattering geometry, and the Raman signals were collected using a 20× Mitutoyo long working distance objective and dispersed by a 1200 mm^{-1} grating. Laser-heating experiments were excited by a Nd:YAG laser (1064 nm) with a power of 5 W. A Mitutoyo 10× (N.A. = 0.26) NIR objective was used to focus the laser and the typical focal spot diameter is about 10 μm. The temperature was determined using the emission spectrum of the black body radiation within the Planck's radiation law [34].

First-principles calculations based on density functional theory (DFT) [35,36] were performed within the generalized gradient approximation (Perdew-Burke-Ernzerhof functional) [37], and the projector augmented-wave method [38,39] as implemented in the VASP code [40,41]. The electron-ion interaction was described with $3s^2 3p^3$ and $4s^2 4p^5$ configurations considered as the valence electrons of P and Br, respectively. Setting the electronic wave functions cutoff energy to 500 eV and Sampling Brillouin zone by Γ-centered k-point meshes with a value of $2\pi \times 0.03\,Å^{-1}$ are to ensure that the convergence criteria for structural optimizations was set to about 1 meV/atom.

III. RESULTS AND DISCUSSION

A. High-pressure experiments of molecular phase

PBr_3 is a colorless liquid at ambient condition and its Raman spectrum is characterized by two stretching modes ω_1(A) and ω_3(E) and two deformation modes ω_2(A) and ω_4(E), which are located at 396 cm^{-1}, 378 cm^{-1}, 160 cm^{-1}, and 115 cm^{-1}, respectively [42]. Among them, ω_3 and ω_4 are twofold degenerate, and the detailed Raman peaks assignments are given in Table S1 [43,44]. In order to know the pressure response of PBr_3, high-pressure Raman measurements of PBr_3 were performed up to 43.9 GPa shown in Fig. 1. It can be seen that a liquid-solid phase transition occurs at about 0.9 GPa evidenced by a sudden narrowing in the full wide at half maximum (FWHM) and the appearance of lattice modes, indicating the crystalized PBr_3 possesses a relatively uniform molecular bonding length and angle than that of liquid phase. This transition is also confirmed by the visual observation of crystallization in the chamber (see Supplemental Material, Fig. S1 [44]). With increasing pressure, except ω_3 band, all other Raman peaks shift to high wavenumber region, suggesting the reduced bond lengths of their corresponding normal vibrations are shortened under external compression. As changes in response of the Raman mode with pressure could provide useful information about phase transitions and chemical changes *et al.* [45–47], which are characterized by missing and splitting of vibrational modes, appearance of new modes, and sudden changes in the slope of the frequency-pressure curve at certain pressure. The Raman frequency-pressure relationships were plotted and given in Fig. S2 [44]. Consistent with the above analysis about the liquid-solid phase transition, sudden slope changes in the curves and appearance of lattice modes are observed at 0.9 GPa. Furthermore, the twofold-degenerated bands ω_3 and ω_4 start to split when the pressure approaches 5.0 and 10.0 GPa, respectively, indicating a pressure-induced lowering of molecular point group symmetry occurs. From the high-pressure Raman spectra and frequency-pressure relationships of PBr_3, taken

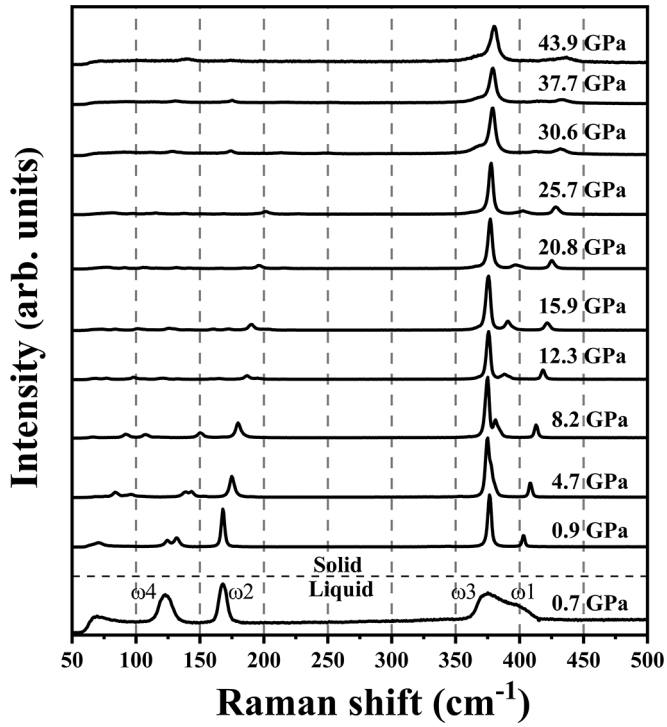

FIG. 1. High-pressure Raman spectra of PBr_3, where ω represents the Raman mode.

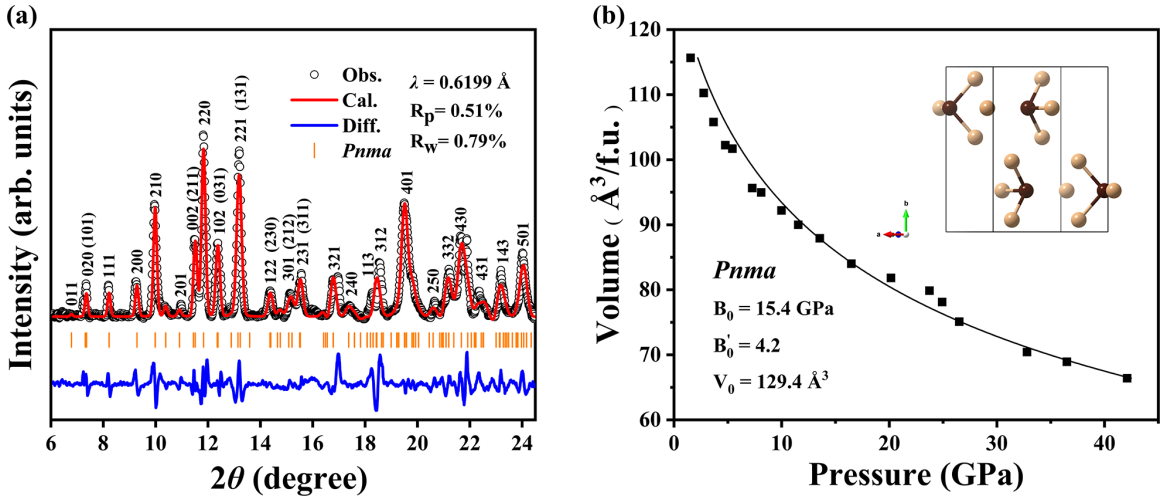

FIG. 2. (a) Rietveld refinement of the crystal structure of *Pnma* phase at 1.5 GPa with a wavelength of 0.6199 Å. The black circles, red curves, and blue curves correspond to the experimental data, Rietveld refinement fits, and residues, respectively. (b) EOS and crystal structure of *Pnma* phase where the square symbols and solid line represent the experimental data and fit, respectively. Brown and beige balls represent the P atoms and Br atoms, respectively.

together, no obvious phase transition could be concluded in the pressure range of 0.9–43.9 GPa.

In order to clarify the crystal structure and the compression behavior of the solid phase, we performed synchrotron XRD measurements of PBr_3 up to 42.1 GPa. The XRD patterns were indexed in terms of an orthorhombic unit cell (space group *Pnma*) with lattice parameters of $a = 7.658$ Å, $b = 9.723$ Å, and $c = 6.218$ Å at 1.5 GPa [Fig. 2(a)]. The *Pnma* phase was characterized as four formula units per unit cell and each P atom is coordinated by three Br atoms. From the evolution of XRD (see Supplemental Material, Fig. S3 [44]), it is obvious that the *Pnma* phase is stabilized to 42.1 GPa, which is consistent with the Raman results. Furthermore, we fitted the equation of state (EOS) of the *Pnma* phase [Fig. 2(b)] and obtained the bulk modulus $B_0 = 15.4$ GPa and pressure derivative $B_0' = 4.2$ by using $V_0 = 129.4$ Å^3 [18].

B. High-pressure experiments of quasi-six-coordinated layered phase

Under high pressure, enthalpy is the main parameter that determines whether phase transitions or chemical reactions occur. However, due to the kinetic barrier, they cannot always be observed in the room-temperature compression process [1]. High temperature can increase the kinetic energy of atoms, thus inducing the system to surpass the energy barrier and stabilize at a relatively lower enthalpy condition. In recent years, laser-heating diamond-anvil-cell technique is an efficient means to provide a high-temperature and pressure environment [48,49]. Using this technique, phenomena such as phase transition and disproportionation could be observed. In this report, PBr_3 was laser heated to about 1800 K at 27.0 GPa, and the corresponding Raman spectrum is given in Fig. 3. Compared to the Raman spectrum of *Pnma* -structured PBr_3 at 27.0 GPa before laser heating, the Raman spectrum of that after laser heating has more and sharper Raman peaks. To qualify the width of the Raman peaks, the FWHM of each Raman peak of PBr_3 before and after laser heating at 27 GPa are shown in Fig. S4 [44]. Except the newly arisen peaks located at 228, 316, and 359 cm^{-1} in $P2_1/c$ phase (after laser heating), the FWHM values of *Pnma* phase are larger than that of $P2_1/c$ phase. The *Pnma* phase of PBr_3 has a character of molecular crystal, and the optical phonon modes are 3N-6=6 where N=4 is the atomic number in each molecular PBr_3. While after laser heating, the number of Raman peaks is almost doubled, suggesting an extended structure or a molecular unit containing more than 4 atoms is built. In addition, P-Br stretching modes ω_1 and ω_3 shift to the low wavenumber region, indicating the P-Br bond is elongated in the newly formed phase. Moreover, the Raman measurements were performed at each step of decompression and shown in Fig. S5 [44]. Compared to the *Pnma* phase, a

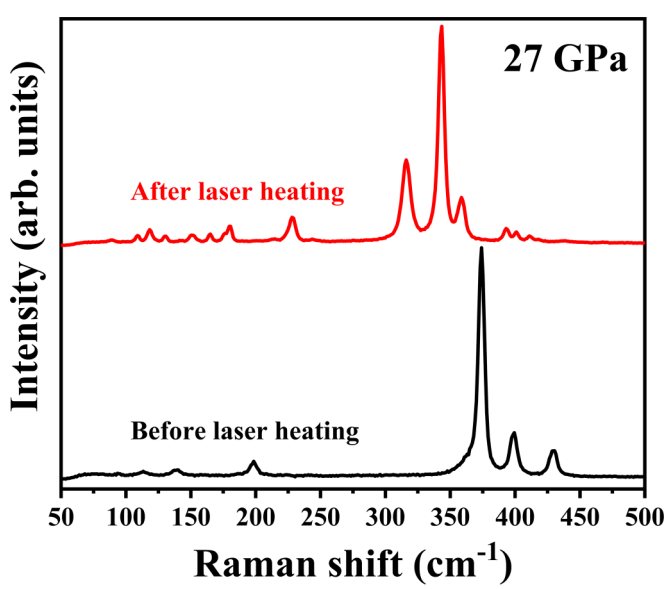

FIG. 3. Raman spectra of PBr_3 before and after laser heating at 27.0 GPa.

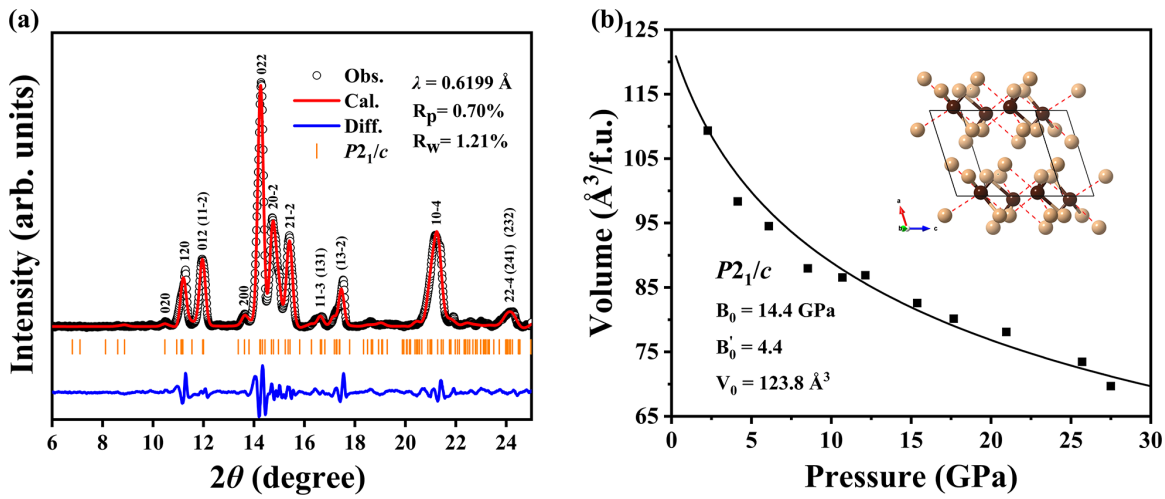

FIG. 4. (a) Rietveld refinement of the crystal structure of phase $P2_1/c$ at 27.0 GPa with a wavelength of 0.6199 Å. The black circles, red curves, and blue curves correspond to the experimental data, Rietveld refinement fits, and residues, respectively. (b) EOS of the $P2_1/c$ phase where the square symbols and solid line represent the experimental data and fit, respectively. Crystal structure of phase $P2_1/c$. Brown and beige balls represent the P atoms and Br atoms, respectively. Red dashed represents longer bonding than that of bicolor line.

softening behavior of a few Raman modes is observed in the new-formed phase, which should be attributed to the existence of stronger intermolecular interaction. Meanwhile, it is obvious that the newly formed phase is stable down to 1.8 GPa and then transforms back to the *Pnma* phase at 1.2 GPa.

In order to know the crystal structure of the new-formed phase of PBr_3, we performed synchrony XRD measurements, and the XRD pattern was collected and indexed as a monoclinic structure (space group $P2_1/c$) with lattice parameters of $a = 5.481$ Å, $b = 8.018$ Å, $c = 6.714$ Å, and $\beta = 107.5375°$ at 27.0 GPa [Fig. 4(a)], which is isostructural with SbI_3 [50,51]. As shown in Fig. 4(b), the $P2_1/c$ phase consists of a single layer of P atoms sandwiched between two layers of Br atoms, and each P atom is coordinated by three nearest-neighboring and three next-nearest-neighboring Br atoms, forming a PBr_6 octahedra. From the previous high-pressure results, it is undoubtedly demonstrated that pressure could induce band-gap closure and metallization in elements and compounds [1,2,4,5,52] and could decrease electronegativities of elements in periodic table (except Tb, Dy, and Ho) [53]. Moreover, for ionic type compounds AX_3, metal element A donates three *p* electrons to X atoms forming an ideal six-coordinated layered structure [21,23–25]. Therefore, it is reasonable that the metallicity of nonmetal element P increases and the electronegativities decrease under high pressure leading to the discovery of quasi-six-coordinated layered structure of PBr_3. The decompressed XRD patterns of $P2_1/c$ phase are shown in Fig. S6 [44] suggesting the $P2_1/c$ phase can be stable down to 1.5 GPa, which is consistent with the previous Raman analysis. In addition, we fitted the EOS of $P2_1/c$ phase in Fig. 4(b) and yield the bulk modulus $B_0 = 14.4$ GPa, pressure derivative $B_0' = 4.4$, and $V_0 = 123.8$ Å^3. Compared to the *Pnma* phase, the increase in the bulk modulus and decrease in V_0 indicates the $P2_1/c$ phase is a close-packed phase.

C. First-principles calculations

To gain a deeper insight into the mechanism of phase transition of PBr_3, we investigated electronic structures of the *Pnma* and $P2_1/c$ phases at 30 GPa (see Fig. 5). Results

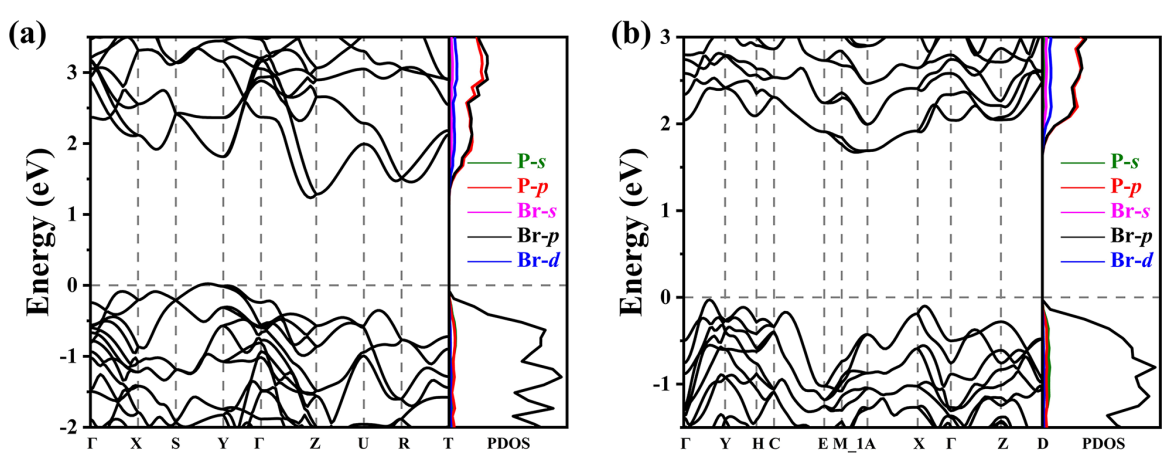

FIG. 5. Calculated electronic band structures (left panel) and partial density of state (right panel) of (a) *Pnma* structure and (b) $P2_1/c$ structure at 30 GPa.

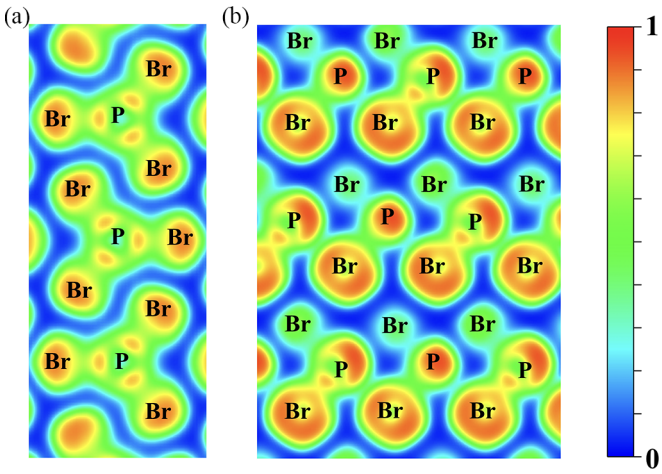

FIG. 6. Electron localization functions within (a) the (h k l) (3.569 0 1) plane of *Pnma* phase and (b) the (h k l) (0 1 0) plane of $P2_1/c$ phase at 30 GPa.

indicate both are indirect gap semiconductors and show a continuous decrease in band gap as the pressure increase (see Supplemental Material, Fig. S7 [44]). The images of the sample chamber (*Pnma* phase) at high pressure were given in Fig. S8 [44]. It can be clearly seen that the color of the sample gradually deepens, which is consistent with the theoretical results of the band gap. Furthermore, the band gap of $P2_1/c$ phase is larger than that of *Pnma* phase in the pressure range of this study (see Supplemental Material, Fig. S7 [44]). The projected density of states (PDOS) of *Pnma* -PBr_3 [see Fig. 5(a)] indicates that valence band is occupied mostly by Br-4 *p* orbital, while the Br-4 *p* and P-3 *p* orbitals show strong hybridization as shown in conduction band. The $P2_1/c$ phase adopts a similar *p* - *p* hybridization with the *Pnma* phase [see Fig. 5(b)]. Moreover, we calculated Bader charges of the two phases, respectively (see Supplemental Material, Table S2 [44]), which indicates that there is no obvious difference between the two phases.

We have calculated electron localization functions (ELFs) of *Pnma* phase [Fig. 6(a)] and $P2_1/c$ phase [Fig. 6(b)], respectively. As shown in Fig. 6(a), it is clear that the localized charge distribution is seen within the molecule PBr_3, which is attributed to the strong P-Br covalent bond. Figure 6(b) displays ELF in the (0 1 0) plane of $P2_1/c$ phase, as a result of the layered atomic distribution, electrons are mainly distributed within the sandwiched layers of P and Br atoms. In addition, P-Br bonds can be divided into three strong and three weak bonds with the bond lengths ranging from 2.26 Å to 2.30 Å and 2.68 Å to 2.80 Å, respectively (see Supplemental Material, Fig. S9 [44]), resulting in a quasi-six-coordinated layer structure of PBr_3. Among them, the strong bonds are relative to primitive P-Br covalent bonds as the *Pnma* phase, and the weak bonds are attributed to noncovalent interactions—pnictogen bonds, which is the result of Coulomb attraction between sites of unequal charge density [54–58]. Recently, scientists found that there are three σ holes that exist in molecule PBr_3, leading to Coulomb attraction between σ holes and atoms characterized by nucleophilicity such as halogen atoms, thus resulting in the generation of pnictogen bonds [59]. In conclusion, the generation of layered phase $P2_1/c$ in PBr_3 is related for two reasons: firstly, high temperature induces an increase in kinetic energy of PBr_3 molecules, leading to greater freedom of movement of the molecules; Secondly, intrinsic σ holes in PBr_3 molecules attract adjacent Br atoms of other PBr_3 molecules by Coulomb force, leading to generation of quasi-six-coordinated layer phase $P2_1/c$.

IV. CONCLUSIONS

To sum up, we systematically investigate the phase transitions of PBr_3 up to 43.9 GPa by a joint high-pressure experimental (Raman scattering, synchrotron XRD, and laser-heating diamond-anvil-cell technology) and theoretical approaches. Upon room temperature compression, a *Pnma* phase is solidified from the liquid PBr_3 at 0.9 GPa and is found to be stable up to 43.9 GPa. Intriguingly, a novel layered phase (space group $P2_1/c$) is generated from the *Pnma* phase at ∼27.0 GPa and ∼1800 K, which is characterized by quasi-six-coordination of P and Br atoms. Furthermore, the electronic band structures PDOS and ELFs of *Pnma* and $P2_1/c$ phases are analyzed, which indicated that the bonds of $P2_1/c$ phase can be divided into covalent bonds and pnictogen bonds. This report realizes the phase diagram of PBr_3, paves a new avenue towards the synthesis of layered vdW trihalides from nonmetal elements and halogens and provides a reference for generation of three-dimensional extension structure from molecules under the influence of pnictogen bonds.

ACKNOWLEDGMENTS

This research was supported by National Key Research and Development Program of China (Grants No. 2021YFA1400503, and No. 2021YFA1400203), the National Natural Science Foundation of China (Grant No. 52090024). The XRD measurements were performed at Beijing Synchrotron Radiation Facility beamline 4W2.

[1] R. J. Hemley, Effects of high pressure on molecules, Annu. Rev. Phys. Chem. **51**, 763 (2000).

[2] H. K. Mao, X. J. Chen, Y. Ding, B. Li, and L. Wang, Solids, liquids, and gases under high pressure, Rev. Mod. Phys. **90**, 015007 (2018).

[3] A. F. Goncharov, V. V. Struzhkin, M. S. Somayazulu, R. J. Hemley, and H.-K. Mao, Compression of ice to 210 Gigapascals: Infrared evidence for a symmetric hydrogen-bonded phase, Science **273**, 218 (1996).

[4] Y. Li, J. Hao, H. Liu, Y. Li, and Y. Ma, The metallization and superconductivity of dense hydrogen sulfide, J. Chem. Phys. **140**, 174712 (2014).

[5] D. Duan, Y. Liu, F. Tian, D. Li, X. Huang, Z. Zhao, H. Yu, B. Liu, W. Tian, and T. Cui, Pressure-induced metallization of

dense $(H_2S)_2H_2$ with high-T_c superconductivity, Sci. Rep. **4**, 6968 (2014).

[6] A. P. Drozdov, M. I. Eremets, I. A. Troyan, V. Ksenofontov, and S. I. Shylin, Conventional superconductivity at 203 K at high pressures, Nature **525**, 73 (2015).

[7] W. Lu, S. Liu, G. Liu, K. Hao, M. Zhou, P. Gao, H. Wang, J. Lv, H. Gou, G. Yang, Y. Wang, and Y. Ma, Disproportionation of SO_2 at High Pressure and Temperature, Phys. Rev. Lett. **128**, 106001 (2022).

[8] V. Iota, C. S. Yoo, and H. Cynn, Quartzlike carbon dioxide: An optically nonlinear extended solid at high pressures and temperatures, Science **283**, 1510 (1999).

[9] T. Kenichi, S. Kyoko, F. Hiroshi, and O. Mitsuko, Modulated structure of solid iodine during its molecular dissociation under high pressure, Nature (London) **423**, 971 (2003).

[10] D. Laniel, T. Fedotenko, B. Winkler, A. Aslandukova, A. Aslandukov, G. Aprilis, S. Chariton, V. Milman, V. Prakapenka, L. Dubrovinsky, N. Dubrovinskaia, A reentrant phase transition and a novel polymorph revealed in high-pressure investigations of CF_4 up to 46.5 GPa, J. Chem. Phys. **156**, 044503 (2022).

[11] C. H. Kronbo, E. Ehrenreich-Petersen, M. Ottesen, F. Menescardi, D. Ceresoli, and M. Bremholm, High-pressure, high-temperature studies of phase transitions in $SrOsO_3$-discovery of a post-perovskite, Inorg. Chem. **61**, 19088 (2022).

[12] A. Tasaka, Electrochemical synthesis and application of NF_3, J. Fluorine Chem. **128**, 296 (2007).

[13] R. E. Brandt, R. C. Kurchin, R. L. Z. Hoye, J. R. Poindexter, M. W. B. Wilson, S. Sulekar, F. Lenahan, P. X. T. Yen, V. Stevanović, J. C. Nino, M. G. Bawendi, and T. Buonassisi, Investigation of bismuth triiodide (BiI_3) for photovoltaic applications, J. Phys. Chem. Lett. **6**, 4297 (2015).

[14] W. Fang, H. Jiang, Y. Zheng, H. Zheng, X. Liang, Y. Sun, C. Chen, H. Xiang, A bilayer interface formed in high concentration electrolyte with SbF_3 additive for long-cycle and high-rate sodium metal battery, J. Power Sources **455**, 227956 (2020).

[15] J. Galy and R. Enjalbert, Crystal chemistry of the VA element trihalides: Lone pair, stereochemistry, and structural relationships, J. Solid State Chem. **44**, 1 (1982).

[16] D. Kurzydłowski, H. B. Wang, I. A. Troyan, M. I. Eremets, Lone-pair interactions and photodissociation of compressed nitrogen trifluoride, J. Chem. Phys. **141**, 064706 (2014).

[17] I. C. Tornieporth-oetting, T. M. Klapötke, Recent developments in the chemistry of binary nitrogen-halogen species, Comments Inorg. Chem. **15**, 137 (1994).

[18] R. Enjalbert, J. Galy, Structure cristalline du tribromure de phosphore à 193 K, Acta Crystallogr. Sect. B **35**, 546 (1979).

[19] E. T. Lance, J. M. Haschke, and D. R. Peacor, Crystal and molecular structure of phosphorus triiodide, Inorg. Chem. **15**, 780 (1976).

[20] R. Enjalbert and J. Galy, Refinement of the structure of arsenic triiodide, Acta Crystallogr. Sect. B **36**, 914 (1980).

[21] J. Trotter and T. Zobel, The crystal structure of SbI_3 and BiI_3, Z. Kristallogr. - Cryst. Mater. **123**, 67 (1966).

[22] M. Ruck, Darstellung und Kristallstruktur von fehlordnungsfreiem Bismuttriiodid, Z. Kristallogr. - Cryst. Mater. **210**, 650 (1995).

[23] M. A. McGuire, H. Dixit, V. R. Cooper, and B. C. Sales, Coupling of crystal structure and magnetism in the layered, ferromagnetic insulator CrI_3, Chem. Mater. **27**, 612 (2015).

[24] S. Tian, J.-F. Zhang, C. Li, T. Ying, S. Li, X. Zhang, K. Liu, and H. Lei, Ferromagnetic van der Waals Crystal VI_3, J. Am. Chem. Soc. **141**, 5326 (2019).

[25] Y. Akahama, S. Endo, and S. Narita, Electrical properties of single-crystal black phosphorus under pressure, Physica B+C **139-140**, 397 (1986).

[26] X.-D. Wen, R. Hoffmann, and N. W. Ashcroft, Benzene under high pressure: a story of molecular crystals transforming to saturated networks, with a possible intermediate metallic phase, J. Am. Chem. Soc. **133**, 9023 (2011).

[27] L. Zhang, Y. Niu, Q. Li, T. Cui, Y. Wang, Y. Ma, Z. He, and G. Zou, Ab initio prediction of superconductivity in molecular metallic hydrogen under high pressure, Solid State Commun. **141**, 610 (2007).

[28] Y. Akahama, H. Kawamura, D. Hausermann, M. Hanfland, and O. Shimomura, New High-Pressure Structural Transition of Oxygen at 96 GPa Associated with Metallization in a Molecular Solid, Phys. Rev. Lett. **74**, 4690 (1995).

[29] Y. Akahama and H. Kawamura, Pressure calibration of diamond anvil Raman gauge to 310 GPa, J. Appl. Phys. **100**, 043516 (2006).

[30] H.-K. Mao, J. Xu, and P. Bell, Calibration of the ruby pressure gauge to 800 kbar under quasi-hydrostatic conditions, J. Geophys. Res. **91**, 4673 (1986).

[31] C. Prescher and V. B. Prakapenka, DIOPTAS: a program for reduction of two-dimensional X-ray diffraction data and data exploration, High Press. Res. **35**, 223 (2015).

[32] B. H. Toby and R. B. Von Dreele, GSAS-II: the genesis of a modern open-source all purpose crystallography software package, J. Appl. Crystallogr. **46**, 544 (2013).

[33] F. Birch, Finite elastic strain of cubic crystals, Phys. Rev. **71**, 809 (1947).

[34] M. Planck, *The Theory of Heat Radiation* (Dover, New York, 1959).

[35] P. Hohenberg and W. Kohn, Inhomogeneous electron gas, Phys. Rev. **136**, B864 (1964).

[36] W. Kohn and L. J. Sham, Self-consistent equations including exchange and correlation effects, Phys. Rev. **140**, A1133 (1965).

[37] J. P. Perdew, K. Burke, and M. Ernzerhof, Generalized Gradient Approximation Made Simple, Phys. Rev. Lett. **77**, 3865 (1996).

[38] P. E. Blöchl, Projector augmented-wave method, Phys. Rev. B **50**, 17953 (1994).

[39] G. Kresse and D. Joubert, From ultrasoft pseudopotentials to the projector augmented-wave method, Phys. Rev. B **59**, 1758 (1999).

[40] G. Kresse and J. Hafner, *Ab initio* molecular dynamics for open-shell transition metals, Phys. Rev. B **48**, 13115 (1993).

[41] G. Kresse and J. Furthmüller, Efficient iterative schemes for ab initio total-energy calculations using a plane-wave basis set, Phys. Rev. B **54**, 11169 (1996).

[42] A. T. Kozulin, A. V. Gogolev, and V. I. Karmanov, Laser raman study of the molecular dynamics of liquid and solid phosphorus tribromide, Sov. Phys. J. **20**, 450 (1977).

[43] A. T. Kozulin, A. V. Gogolev, and S. G. Shishkin, Appearance of Intermolecular Interaction in the Vibrational Spectra of Polyatomic XY_3 Molecules, Sov. Phys. J. **20**, 454 (1977).

[44] See Supplemental Material at http://link.aps.org/supplemental/10.1103/PhysRevResearch.5.033164 for Raman frequencies and assignments for *Pnma* phase of PBr_3; images of the sample

chamber at 0.2 and 0.7 GPa; Raman frequency-pressure curves of *Pnma* phase of PBr_3; High-pressure XRD patterns of the *Pnma* phase up to 42.1 GPa; The FWHM of each Raman peak of PBr_3 before and after laser heating at 27 GPa; Raman spectra of the $P2_1/c$ PBr_3 in decompression; Evolution of XRD patterns for phase $P2_1/c$ as a function of pressure; The band gap of the *Pnma* and $P2_1/c$ phases as a function of pressure; Images of the sample chamber (*Pnma* phase) at high pressure; Bader charges of *Pnma* and $P2_1/c$ phases at 25 GPa; ELF within the intralayer plane of $P2_1/c$ phase at 25 GPa.

[45] R. J. Hemley, H. K. Mao, P. M. Bell, and B. O. Mysen, Raman Spectroscopy of SiO_2 Glass at High Pressure, Phys. Rev. Lett. **57**, 747 (1986).

[46] G. A. Kourouklis, A. Jayaraman, and G. P. Espinosa, High-pressure Raman study of CeO_2 to 35 GPa and pressure-induced phase transformation from the fluorite structure, Phys. Rev. B **37**, 4250 (1988).

[47] G. Li, X. Chen, Y. Gan, F. Li, M. Yan, F. Ye, S. Pei, Y. Zhang, L. Wang, H. Su, J. Dai, Y. Chen, Y. Shi, X.W. Wang, L. Zhang, S. Wang, D. Yu, F. Ye, J. W. Mei, and M. Huang, Raman spectroscopy evidence for dimerization and Mott collapse in α-$RuCl_3$ under pressures, Phys. Rev. Mater. **3**, 023601 (2019).

[48] A. Jayaraman, Diamond anvil cell and high-pressure physical investigations, Rev. Mod. Phys. **55**, 65 (1983).

[49] Y. Meng, R. Hrubiak, E. Rod, R. Boehler, and G. Shen, New developments in laser-heated diamond anvil cell with in situ synchrotron x-ray diffraction at high pressure collaborative, Rev. Sci. Instrum. **86**, 072201 (2015).

[50] S. Pohl and W. Saak, Zur Polymorphie von Antimontriiodid. Die Kristallstruktur von monoklinem SbI_3, Z. Kristallogr. **169**, 177 (1984).

[51] H. C. Hsueh, K. Chen Roger, H. Vass, S. J. Clark, G. J. Ackland, W. C. K. Poon, and J. Crain, Compression mechanisms in quasimolecular XI_3 (X = As, Sb, Bi) solids, Phys. Rev. B **58**, 14812 (1998).

[52] M. Okajima, S. Endo, Y. Akahama, and S. Narita, Electrical investigation of phase transition in black phosphorus under high pressure, Jpn. J. Appl. Phys. **23**, 15 (1984).

[53] M. Rahm, R. Cammi, N. W. Ashcroft, and R. Hoffmann, Squeezing all elements in the periodic table: electron configuration and electronegativity of the atoms under compression, J. Am. Chem. Soc. **141**, 10253 (2019).

[54] T. Clark, M. Hennemann, J. S. Murray, and P. Politzer, Halogen bonding: The σ-hole, J. Mol. Model **13**, 291 (2007).

[55] S. Scheiner, The pnicogen bond: Its relation to hydrogen, halogen, and other noncovalent bonds, Acc. Chem. Res. **46**, 280 (2013).

[56] L. Brammer, Halogen bonding, chalcogen bonding, pnictogen bonding, tetrel bonding: Origins, current status and discussion, Faraday Discuss. **203**, 485 (2017).

[57] K. T. Mahmudov, A. V. Gurbanov, V. A. Aliyeva, G. Resnati, and A. J. L. Pombeiro, Pnictogen bonding in coordination chemistry, Coord. Chem. Rev. **418**, 213381 (2020).

[58] I. Alkorta, J. Elguero, and A. Frontera, Not only hydrogen bonds: Other noncovalent interactions, Crystals **10**, 180 (2020).

[59] P. R. Varadwaj, A. Varadwaj, H. M. Marques, and K. Yamashita, The phosphorous bond, or the phosphorous-centered pnictogen bond: The covalently bound phosphorous atom in molecular entities and crystals as a pnictogen bond donor, Molecules **27**, 1487 (2022).